Effect of doping and lattice dynamics in competing structural phases of $LaSb_2$

Jinwoong Kim,[1,2] Reiley Dorrian,[3] Adrian Llanos,[3] Joseph Falson,[3,4] and Nicholas Kioussis[1]
[1]*Department of Physics and Astronomy, California State University, Northridge, California 91330, USA*
[2]*Korea Institute for Advanced Study, Seoul 02455, Republic of Korea*
[3]*Department of Applied Physics and Materials Science, California Institute of Technology, Pasadena, California 91125, USA*
[4]*Institute for Quantum Information and Matter, California Institute of Technology, Pasadena, California 91125, USA*

(Received 4 August 2025; accepted 23 February 2026; published 17 March 2026)

The layered rare-earth diantimonides, RSb_2, (R = lanthanide element) composed of Sb square-net sheets exhibit diverse structural phases with distinct stacking configurations which can be tuned by the growth temperature, stoichiometry, and pressure. The recent discovery by Llanos *et al.* [Nano Lett. **24**, 8518 (2024)] of a novel monoclinic polymorph of $LaSb_2$ raises the important question as to why $LaSb_2$ has been synthesized in the orthorhombic phase in previous experimental studies. We have employed first-principles electronic structure calculations to investigate the effect of charge doping and phonon entropy on the relative stability between four competing structural phases of $LaSb_2$: the $SmSb_2$-type, the $YbSb_2$-type, the MBE-grown monoclinic, and our novel theoretically predicted orthorhombic structures (space group No. 58, *Pnnm*). The calculations reveal that the $SmSb_2$-type orthorhombic phase is stabilized by electron doping that can presumably occur during bulk growth conditions such as Sb-rich flux, intrinsic vacancy formation, etc. However, the phonon entropy is found to reduce the free energy of the monoclinic phase faster than that of the orthorhombic phase with increasing temperature, indicating that the monoclinic phase becomes more stable at high temperatures. We also present the dynamical instabilities in two well-known structures with or without strain that qualitatively explain the pressure-dependent charge density waves of $LaSb_2$. This research aims to shed light on the microscopic mechanisms underlying the complex and competing structural phases and resulting transitions in the family of RSb_2 systems.

DOI: 10.1103/t4m3-jjdn

I. INTRODUCTION

The binary rare-earth metal diantimonides RSb_2 (R = lanthanide element) are a family of layered materials [1–3], consisting of two-dimensional Sb square-net sheets sandwiched between two R-Sb corrugated layers, which form quintuple layer (QL) blocks [4], stacked along the [001] direction. The layered RSb_2 exhibits a wide range of competing electronic phases, including superconductivity (SC) [5–9], charge density waves (CDWs) [10–13], topological states [14,15], and magnetism [14,16,17], which can be tuned through pressure, temperature, and chemical substitution of the R by another R element or Sb by a chalcogen. Equally important are the multiple distinct crystal structures exhibited throughout the family, corresponding to unique stacking configurations [4,18–20] that depend sensitively on the growth temperature, stoichiometry, and pressure, resulting in a variety of structural phase transitions between phases of distinct electronic properties.

For instance, both the $LaSb_2$ and $CeSb_2$ systems synthesized in the orthorhombic $SmSb_2$-type structure [2,21,22] exhibit hysteretic anomalies in the temperature-dependent resistivity, which are often attributed to CDW in the literature [11,12]. Applying pressure suppresses the CDWs in both systems [11,12] while enhancing the superconducting critical temperature in $LaSb_2$ [4] and revealing a novel pressure-induced SC in $CeSb_2$ [8]. The SC was speculated to be related to a different high-pressure phase, the $YbSb_2$-type structure [1] of $LaSb_2$, resulting from a pressure-induced structural phase transition from the original $SmSb_2$-type phase [8,12]. Hence, it is crucial to understand the metastable structural phases and potential structural phase transitions between them for further investigations of the CDW and SC.

Recently, molecular beam epitaxy (MBE) studies and our complementary first principles electronic structure calculations reported the discovery of a novel monoclinic polymorph of $LaSb_2$ stabilized in thin films (space group No. 12, $C2/m$), a shear-deformed variant of the $YbSb_2$ structure (space group No. 63, *Cmcm*) [4]. This is in contrast to the well-known orthorhombic bulk crystal structure grown with the self-flux method [23–25], similar to the $SmSb_2$ structure (space group No. 64, *Cmca*) [2]. Interestingly, the calculations revealed that the monoclinic phase is the ground state with a lower total energy than the orthorhombic $SmSb_2$-type phase. This result raises the intriguing question of the underlying origin of the orthorhombic $SmSb_2$-type structure of $LaSb_2$ synthesized in previous experimental studies.

The objective of this work is to employ first principles electronic structure and lattice dynamics calculations to investigate the effects of (i) charge doping, (ii) hydrostatic pressure, and (iii) phonon entropy on the relative stability of the various structures and the resulting phase transitions. The calculations reveal that electron doping, which can occur under Sb-rich growth conditions, may stabilize the orthorhombic $SmSb_2$-type structure. However, the phonon entropy contribution to the free energy is found to stabilize the monoclinic phase with

increasing temperature. In Sec. II we outline the methodology. In Sec. III A we compare the complex energy landscape of the relative shifts of two QLs for $R\mathrm{Sb}_2$ for R = Sm, Yb, and La, which allows us to determine the distinct ground state crystal structures of these three lanthanide members. In Sec. III B we discuss the effect of electron/hole doping on the stability of the four LaSb_2 phases as well as the effect of hydrostatic pressure. In Sec. III C we present the lattice dynamics and their contribution to the temperature-dependent free energies of the competing structural phases. In Sec. III D the dynamical instability of the well-known structures is discussed. The results are summarized in Sec. IV.

II. METHODOLOGY

First-principles calculations are performed with the Vienna *Ab Initio* Simulation Package (VASP) [26,27]. The pseudopotential and wave functions are represented within the projector augmented wave method [28,29]. The valence configurations are $5s^25p^66s^25d^1$ and $5s^25p^3$ for La and Sb, respectively. Assuming the paramagnetic phase, which is the phase under the experimental growth conditions, the f bands are treated as core states for the cases of R = Sm and Yb, where the valence configurations are $5s^25p^66s^25d^1$ and $6s^25p^6$, respectively. The plane wave cutoff energy is set to 500 eV, and $16 \times 16 \times 6$ k-point mesh is used in the momentum space sampling. The crystal structures are optimized within energy convergence criteria of 10^{-5} eV. The dynamical matrices are calculated using VASP-PHONOPY [30,31] interface with the finite displacement method in $2 \times 2 \times 1$ supercell (16 La and 32 Sb atoms) structures with $8 \times 8 \times 6$ k-point mesh. Finite-temperature phonon effects are additionally examined using the special displacement method developed by Zacharias and Giustino [32–34] in $2 \times 2 \times 1$ supercell structures. The equilibrium atomic positions are fixed to those of the relaxed structures [35].

Additional details, including the relaxed crystal structures of the Sm-type, Yb-type, Yb-mono, and Yb-alt phases, as well as supplementary figures and tables illustrating the effects of charge doping and pressure on the lattice parameters, are provided in the Supplemental Material [36].

III. RESULTS AND DISCUSSION

A. Structural stability and stacking order of $R\mathrm{Sb}_2$ (R = Sm, Yb, La)

In this section, we demonstrate that the various structural phases of $R\mathrm{Sb}_2$ are linked to distinct stacking configurations between two QL blocks, each consisting of two weakly bonded R-Sb corrugated layers sandwiching a two-dimensional Sb square net sheet shown in Fig. 1(d). Since each stacking configuration of two building blocks causes a lateral shift of one QL relative to the other, the entire structure exhibits a shear deformation leading to a monoclinic lattice, unless the relative shifts between successive QLs are compensated as in the orthorhombic SmSb_2- or YbSb_2-type phases. Employing this approach, we predicted a novel LaSb_2 orthorhombic phase (space group No. 58, *Pnnm*), which is close in energy (4 meV/La) to the monoclinic ground state [4].

The structural stability and stacking order of the various crystal structures of three prototype $R\mathrm{Sb}_2$ members (R = Sm, Yb, La) can be understood using the construction of relative lateral shift of two QL blocks, suspended in vacuum, with subsequent relaxation of the atomic positions normal to the slab, that we reported for LaSb_2 [4]. The upper QL is shifted relative to the lower one by a lateral displacement vector, $\vec{d} = d_x\vec{a}_1 + d_y\vec{a}_2 = (d_x, d_y)$, where the calculated equilibrium in-plane lattice constants, $|\vec{a}_1| = |\vec{a}_2|$, for a relaxed single QL slab are 4.379 Å, 4.417 Å, and 4.501 Å for R = Sm, Yb, and La, respectively [37].

The energy landscapes of the two building blocks on the two-dimensional (d_x, d_y) displacement space for SmSb_2, YbSb_2 and LaSb_2 are shown in Figs. 1(a), 1(b), and 1(c), respectively. The global energy minimum for SmSb_2, denoted by $S^{\pm}$ occurs at $(d_x, d_y) = (\pm\frac{1}{4}, \pm\frac{1}{4})$ and its C_4 symmetric copies. Naturally, the crystal structure of SmSb_2, shown in Fig. 1(e), consists of building blocks with a stacking sequence $\cdots S^+S^-S^+S^-\cdots$, where successive adjacent QL blocks are shifted by $(\frac{1}{4}, \frac{1}{4})$ and $(-\frac{1}{4}, -\frac{1}{4})$ displacements, respectively.

However, the energy landscape for YbSb_2 displayed in Fig. 1(b) shows that the global energy minimum occurs at the distinct lateral displacement, $(0, \pm\frac{1}{2})$, denoted by Y^0. The observed orthorhombic crystal structure of YbSb_2 can be derived from the predicted stacking sequence $\cdots Y^0Y^0Y^0Y^0\cdots$, of consecutive displaced QL blocks, as illustrated in Fig. 1(f). Both the SmSb_2 and YbSb_2 structures preserve orthorhombicity because the successive lateral displacements are compensated.

The energy landscape for LaSb_2, displayed in Fig. 1(c) shows four global energy minima at the off-symmetry points, $Y^{\pm} = (\pm 0.1, 0.5)$, resulting in two possible periodic stacking sequences of adjacent QL blocks. The first one consists of a repeating Y^+ stacking, $\cdots Y^+Y^+Y^+Y^+\cdots$, illustrated in Fig. 1(g), where the noncompensating $\hat{x}$ displacement leads to shear deformation of the out-of-plane lattice vector, rendering the system monoclinic, which is the ground state. This result is consistent with the recently synthesized monoclinic phase in MBE growth, where the calculated lattice constants and monoclinic angle agree well with the experimental parameters within 1% of error [4]. The second sequence, $\cdots Y^+Y^-Y^+Y^-\cdots$, with a compensated displacement [Fig. 1(h)] results in a newly predicted orthorhombic phase (space group No. 58, *Pnnm*) which is only 4 meV/La higher in energy than the ground state monoclinic phase, suggesting a possible coexistence of the two phases.

These three energy landscapes are representative cases regarding the distinct stacking configurations of the $R\mathrm{Sb}_2$ family of materials, characterizing the structural properties. In this sense, the various $R\mathrm{Sb}_2$ structures can be classified into these three groups; SmSb_2-type, YbSb_2-type, and LaSb_2-type, based on the energy map showing qualitative differences in the overall shapes. Thus, it is natural to label the monoclinic phase of LaSb_2 as LaSb_2-type. However, to keep the notation consistent with our previous work [4] throughout the remaining of this manuscript, we denote the structures of LaSb_2 of the SmSb_2 (YbSb_2) type with repeating stacking sequences of $\cdots S^+S^-\cdots$ ($\cdots Y^0Y^0\cdots$) as Sm-type (Yb-type) phase. In addition, the LaSb_2 structure with monoclinic- ($\cdots Y^+Y^+\cdots$)

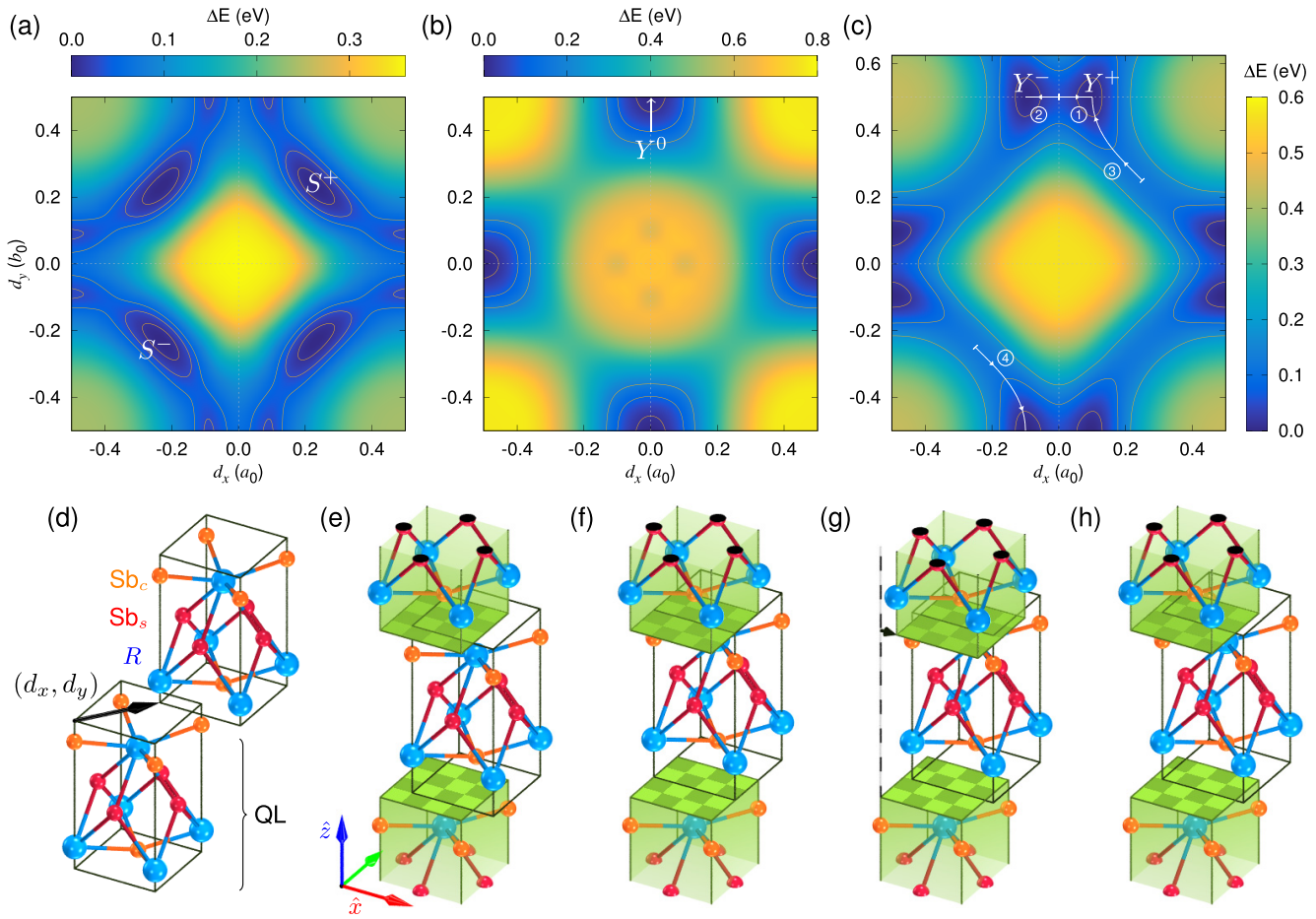

FIG. 1. Energy landscape of the relative lateral displacement, (d_x, d_y), of two QL RSb$_2$ block slabs suspended in vacuum, shown in panel (d), for R = (a) Sm, (b) Yb, and (c) La, respectively. Each block consists of two weakly bonded R-Sb corrugated layers sandwiching a two-dimensional Sb square net sheet. The global energy minima for SmSb$_2$, YbSb$_2$, and LaSb$_2$ are denoted by $S^{\pm} = (\pm 1/4, \pm 1/4)$, $Y^0 = (0, 1/2)$, and $Y^{\pm} \sim (\pm 1/10, 1/2)$, respectively. Periodic stacking sequence of QL building blocks (where green checker grid displays the lateral shifts between two adjacent QL) of $\cdots S^+S^-S^+S^- \cdots$, $\cdots Y^0Y^0Y^0Y^0 \cdots$, $\cdots Y^+Y^+Y^+Y^+ \cdots$, and $\cdots Y^+Y^-Y^+Y^- \cdots$, of the (e) orthorhombic SmSb$_2$ structure, (f) orthorhombic YbSb$_2$ structure, (g) Yb-like monoclinic structure of LaSb$_2$, and (h) Yb-like orthorhombic (Yb-alt) structure of LaSb$_2$, respectively.

and alternating-stacking ($\cdots Y^+Y^- \cdots$) are referred to as Yb-mono and Yb-alt phases, respectively.

Interestingly, we find that the previously synthesized well-known Sm-type structure of LaSb$_2$, consisting of building blocks with stacking sequence $\cdots S^+S^-S^+S^- \cdots$, appears as a saddle point [Fig. 1(c)] with a total energy of 29 meV/La higher than the ground state monoclinic structure. Although the energy landscape may develop a dip at $S^{\pm}$ through additional distortion of QLs inside the bulk, this suggests a potential dynamical instability of the Sm-type LaSb$_2$ stucture where the stacking position slips down the energy landscape from $S^+ \to Y^+$ and $S^- \to Y^-$, along the paths marked as ③ and ④, in Fig. 1(c), respectively. The resistivity anomaly of the Sm-type LaSb$_2$ phase [11,12], attributed to CDW, disappears under pressure due to a potential structural phase transition. The Yb-type phase, another well-known structure in this family of materials, was proposed as the high-pressure state of LaSb$_2$, supported by first-principles calculations, where the predicted transition pressure, 5 kbar, agrees well with experiment [12]. As shown in Fig. 1(c) the stacking position Y^0 of the Yb-type structure is a saddle point for LaSb$_2$ and a dynamical instability ($Y^0 \to Y^{\pm}$), paths ① or ② is expected as well.

The aforementioned results of saddle point stacking indicate the importance of comprehending the stability of lattice dynamics in the competing and complex structural phases of LaSb$_2$. In the following sections, we discuss the effect of doping, lattice dynamics, and dynamical instabilities of the four structural phases of LaSb$_2$.

B. Effect of doping

The MBE-grown LaSb$_2$ is crystallized in the monoclinic phase, which was also found to be the ground state in the first-principles calculations [4]. This raises the question how the widely observed orthorhombic Sm-type phase has been synthesized so far. To understand the origin, we conduct first-principles electronic structure calculations on the effect of charge doping. Note that, throughout this paper, the unit of charge doping concentration is given per formula unit (one La atom and two Sb atoms), unless stated otherwise. Figure 2(a) shows the relative total energies of the four phases versus

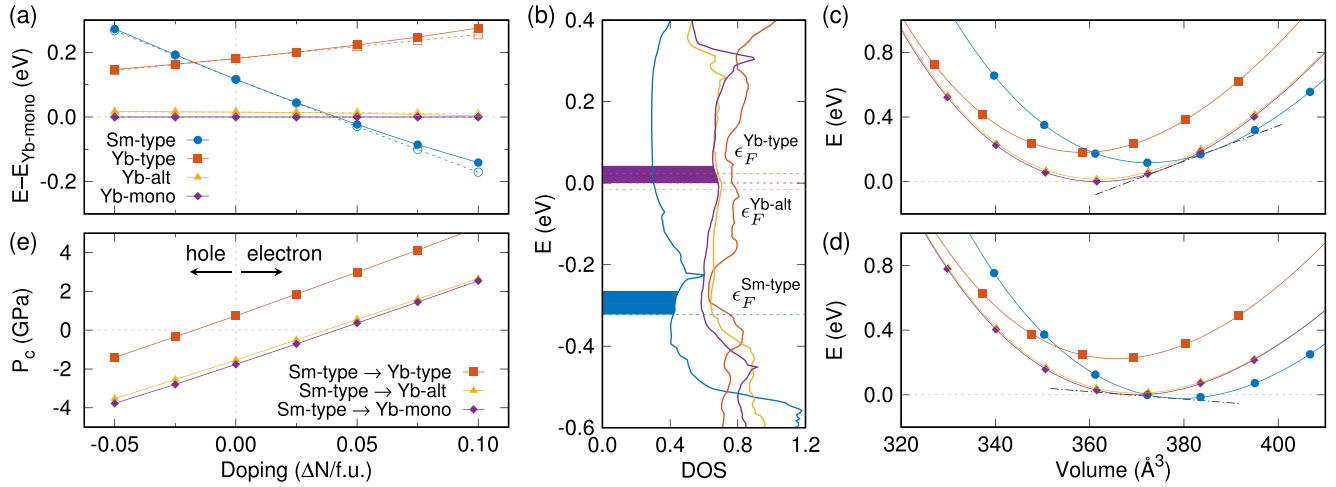

FIG. 2. (a) Total energies of the four phases of $LaSb_2$ relative to the Yb-mono phase as a function of doping. Closed (open) symbols indicate that the crystal structures are relaxed (fixed). (b) Electronic density of states of the four phases of $LaSb_2$ aligned to the semi-core states, $5s^2$ of La atom. The relative positions of the Fermi energies are denoted by the horizontal dashed lines, where the zero energy is set to the Fermi level of the Yb-mono phase. Shaded regions indicate the chemical potential shift upon +0.05 electron doping for the Sm-type (blue) and Yb-mono (purple) phases. Total energies of the four phases $LaSb_2$ as a function of volume for the (c) pristine and (d) +0.05 electron doped cases. The zero energy is set to the minimum energy of the Yb-mono phase. The dotted-dashed lines denote the common tangential of the Sm-type and Yb-mono phases, indicating an enthalpy-conserved structural transition path. (e) Critical hydrostatic pressure for the structural transition from the Sm-type to the other phases versus electron doping.

electron/hole doping per unit cell, where, as alluded earlier, the Yb-mono phase is the ground state at zero doping. Interestingly, under electron doping, the relative total energy of the Sm-type phase decreases linearly and becomes the ground state beyond ∼0.04 electron doping. In sharp contrast, the relative energy of the Yb-type increases linearly with doping, while that of the Yb-alt depends weakly on doping. The solid (dashed) lines in Fig. 2(a) are results with (without) structural relaxation, showing that the effect of structural relaxation is negligible.

The different trends of the total energy of the four $LaSb_2$ phases upon doping can be simply understood in terms of the change of electronic energy with shift of the corresponding Fermi energy. The electronic part of the total energy of the αth phase at zero temperature can be written as

$$E_e^\alpha = \int_{-\infty}^{\epsilon_F^\alpha} \epsilon n^\alpha(\epsilon) d\epsilon, \tag{1}$$

where n^α and ϵ_F^α are the density of states and the Fermi energy of the αth phase. The shift of the chemical potential of the αth phase with doping is

$$\mu^\alpha \simeq \epsilon_F^\alpha + \Delta N / n^\alpha \left(\epsilon = \epsilon_F^\alpha\right), \tag{2}$$

where ΔN indicates the change of number of electrons. The change of total electronic energy is then written as

$$\Delta E_e^\alpha \simeq \epsilon_F^\alpha \Delta N. \tag{3}$$

Consequently, the relative change of total energies between the αth and βth phases is determined by the relative positions of the corresponding Fermi levels,

$$\Delta E_e^\alpha - \Delta E_e^\beta \simeq \left(\epsilon_F^\alpha - \epsilon_F^\beta\right) \Delta N. \tag{4}$$

Figure 2(b) shows the electronic density of states of the four $LaSb_2$ structures and the corresponding positions of the Fermi levels, where the Sm-type phase has significantly lower Fermi level resulting in stabilization upon electron doping. Therefore, this mechanism reconciles the seemingly contradictory experimental findings, where recent MBE growth studies of thin films reported the newly synthesized Yb-mono phase [4] in contrast to the previously reported Sm-type phase of $LaSb_2$ grown with self-flux method [23,24]. The typical Sb-rich growth conditions of bulk $LaSb_2$ which occurs within a liquid flux of Sb may hinder charge neutrality and hence stabilize the metastable orthorhombic Sm-type phase.

Another open question is the structural phase of $LaSb_2$ under hydrostatic pressure, which is considered to be relevant to SC and the disappearance of CDW-like transport anomalies above 5 kbar [4,8,12]. As will be discussed in Sec. III D, the proposed high-pressure Yb-type phase exhibits dynamical instability over a wide pressure range. Therefore, it is unlikely that the Yb-type structure corresponds to the actual high-pressure phase. To gain further insight into the pressure-induced structural transition, we revisit the total energy-pressure relationship while accounting for the effects of charge doping. Figures 2(c) and 2(d) display the total energy of the four $LaSb_2$ phases versus volume under zero and +0.05 electron doping, respectively. The solid lines are fits to the Birch-Murnaghan equation of state [38,39]. In the pristine case, the ground state is the Yb-mono phase and the tangential line between the Yb-mono and Sm-type denotes the enthalpy-preserved structural transition path. The positive slope yields a negative pressure, indicating that the transition can occur under tensile stress. In contrast, for the +0.05 electron-doped case [Fig. 2(d)], the total energy curve of the Sm-type shifts down and becomes the ground state. We predict that the structural transition from

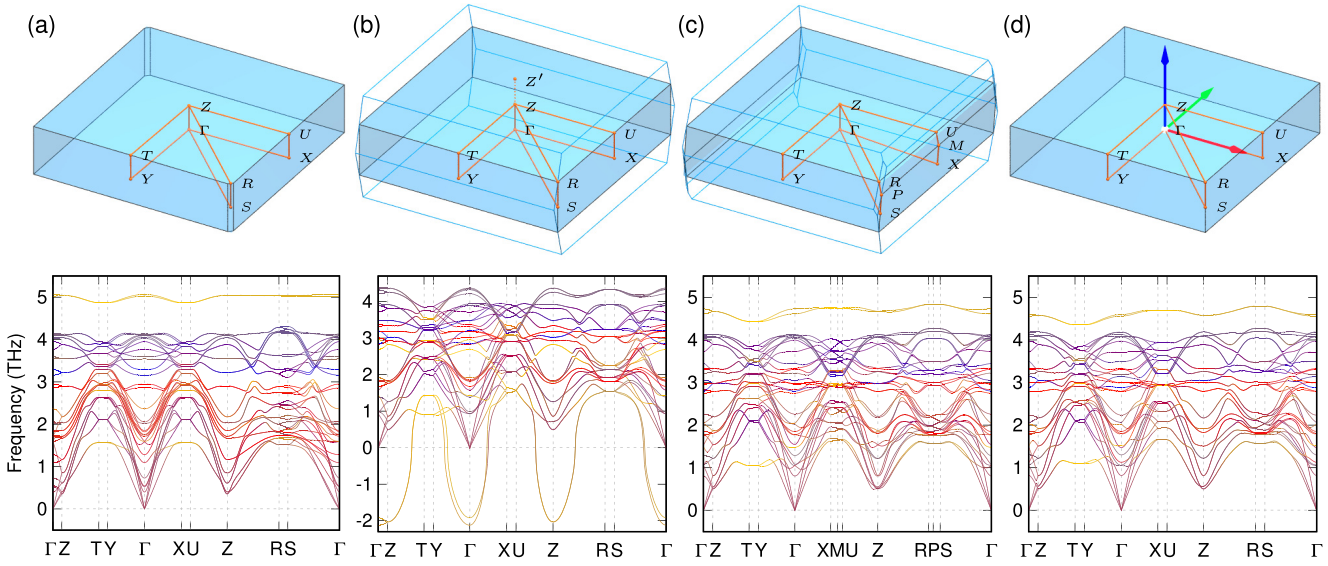

FIG. 3. Phonon band structures of the (a) Sm-type, (b) Yb-type, (c)Yb-mono, and (d) Yb-alt $LaSb_2$ phases at the equilibrium volumes. Upper panels: Corresponding Brillouin zones (BZ) of the four crystal structures consisting of two QLs (four La and eight Sb atoms) that are primitive cells for the (a) Sm-type and (d) Yb-alt phases, but conventional cells for the (b) Yb-type and (c) Yb-mono phases. The first BZs for the (b) Yb-type and (c) Yb-mono phases are also shown with blue lines. Lower panels: Calculated phonon bands, plotted along the high symmetry lines in the BZs, where blue, yellow, and red phonon bands denote projection on the La, Sb_c, and Sb_s atoms, respectively. Negative phonon frequencies for the Yb-type structure in panel (b) indicate dynamical instability.

the Sm-type to the Yb-mono phase occurs at 0.4 GPa. Upon increasing the doping from 0 to 0.05 electrons, the transition pressure from the Sm-type to Yb-type phase increases from 0.7 to 3.0 GPa. In the doping range ($\gtrsim$0.04 electrons) where the Sm-type becomes the ground state, the transition pressure to the Yb-type substantially exceeds the experimentally measured pressure of ∼0.5 GPa. Therefore, we propose that the Yb-mono phase is the high pressure state of $LaSb_2$, rather than the Yb-type phase under electron-rich growth conditions.

Figure 2(e) shows the calculated transition pressure as a function of doping from the Sm-type phase to the other three phases. The experimentally measured threshold pressure of ∼0.5 GPa is then inversely mapped to the corresponding doping levels, which are approximately 0.053 and 0.049 electrons for the Yb-mono and Yb-alt phases, respectively. The shaded area in Fig. 2(b) illustrates that under 0.05 electron doping for the Sm-type and Yb-mono phases the corresponding changes of chemical potential are 0.06 eV and 0.04 eV, respectively. Therefore, an interesting open question is whether a *reciprocal* structural phase transition from the Sm-type to the Yb-mono can be triggered via a gate voltage which introduces hole carriers that will in turn stabilize the Yb-mono phase again. Because of the screening effect, the additional carriers would be concentrated on the surface and the structural transition may locally occur in the vicinity of the surface.

C. Phonon entropy

Figure 3 shows the calculated phonon band structures (lower panels) along the high symmetry lines in the Brillouin zones (BZs) for the (a) Sm-type, (b) Yb-type, (c) Yb-mono, and (d) Yb-alt phases of $LaSb_2$ at the equilibrium volumes. The upper panels show the BZs of the four structures. Note that the stacking periods of $\cdots Y^0 \cdots$ for the Yb-type and of $\cdots Y^+ \cdots$ for the Yb-mono phases are half compared to those of $\cdots S^+S^- \cdots$ for the Sm-type and of $\cdots Y^+Y^- \cdots$ for the Yb-alt phases. As a result, the Yb-type and Yb-mono phases exhibit half-sized primitive cells and hence doubled first BZs, denoted with the blue solid lines in Figs. 3(b) and 3(c). Thus, to compare the phonon bands between the structures, we used common-size cells consisting of two QL with four La and eight Sb atoms.

The blue, yellow, and red phonon bands denote projections on the La, Sb_c, and Sb_s, respectively [see Fig. 1(d) for the labels]. The acoustic modes consist of blended contributions. Overall, the Sb_s-derived (red) optical modes are softer than the La-derived (blue) branches, although La is heavier than Sb, indicating that the bonding involving La atoms is stiffer than that of Sb_s atoms. The Sb_c-derived (yellow) phonon branches in the lower frequency range which appear along the high symmetry $T-Y$ line correspond to vertical Sb_c vibrations. The other Sb_c-derived (yellow) bands above 4.5 THz, corresponding to both in-plane and out-of-plane Sb_c vibrations, are well detached from the major phonon bands except for the Yb-type, where those modes exhibit imaginary frequency along the $\Gamma-Z$ symmetry line. The dynamic instability of the Yb-type phase and its relation with the saddle-point stacking will be discussed in detail in Sec. III D.

One important issue related to the phonon dispersion is the temperature-dependent relative stability between the various structural phases in addition to the charge doping effect. Namely, even though the zero-temperature energy of the Yb-mono phase is predicted to be lower than the commonly synthesized Sm-type phase, the question remains whether the

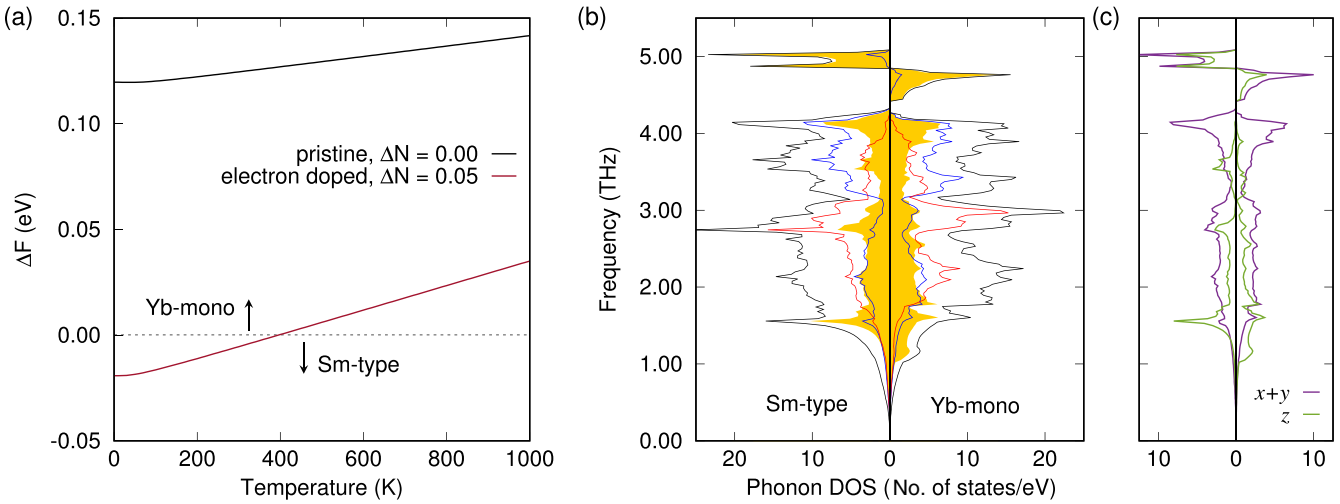

FIG. 4. Phonon free energies and relative stability of Sm-type and Yb-mono phases upon temperature and doping. (a) Difference of free energies between the Sm-type and Yb-mono phases of $LaSb_2$, $\Delta F = F_{\text{Sm-type}} - F_{\text{Yb-mono}}$ for the undoped (0) and electron doped (0.05) cases. Negative (positive) values indicate that the Sm-(Yb-mono) type is the ground state. (b), (c) Projected phonon density of states for the Sm-type (left panels) and Yb-mono (right panels) phases. The blue line, yellow shaded area, and red line in panel (b) denote atomic site-projected phonon DoS on the La, Sb_c, and Sb_s atoms, respectively. The purple and green curves in panel (c) denote in-plane and out-of-plane projected phonon DoS on the Sb_c atoms, respectively.

phonon entropy at T $\neq$ 0 may affect the total free energy and stabilize the Sm-type phase at higher temperatures, during the growth and annealing process [40].

To investigate the temperature-dependent relative stability between the four phases, we have calculated the phonon contribution to the free energy given by

$$F(T) = E_0 + \frac{1}{2}\sum_{\boldsymbol{q}n} \hbar\omega_{\boldsymbol{q}n} + \sum_{\boldsymbol{q}n} k_B T ln(1 - e^{-\hbar\omega_{\boldsymbol{q}n}/k_B T}), \quad (5)$$

where E_0 is the total energy within the Born-approximation [41], the second term is the zero-point phonon energy, and the third term describes the contribution of the phonon entropy. The zero-point energy contribution, $F(T = 0) - E_0$, is found to negligibly affect the relative stability of $LaSb_2$.

Figure 4(a) shows the difference of free energies between the Sm-type and Yb-mono phases, $\Delta F = F_{\text{Sm-type}} - F_{\text{Yb-mono}}$ as a function of temperature for the undoped (0.0) and electron doped (+0.05) cases. For the undoped case we find that the free energy of the Yb-mono is lower than that of Sm-type regardless of temperature. The phonon entropy thus stabilizes more the Yb-mono than the Sm-type, indicating that the phonon entropy is not the origin of stabilizing the Sm-type phase during the bulk sample growth. However, under 0.05 electron doping (red curve) the calculations reveal a crossover from the Sm-type to the Yb-mono phase with increasing temperature at about 430 K, reflecting a change in the relative thermodynamic stability driven by finite-temperature effects. In the context of sample growth, this thermodynamic competition determines which phase is preferentially stabilized under the growth conditions, without requiring a specific transition pathway between fully formed structures. In contrast, for a post-growth transformation of an existing Sm-type sample into the Yb-mono phase, the detailed kinetic pathways and the associated activation barriers would become important, and their characterization remains an open question for future experimental and theoretical studies. We note that the phonon entropy plays a crucial role in $CeSb_2$, where the structural phase is indeed determined by the sample growth temperature [20]. These results indicate the importance of both effects of charge doping and phonon entropy in stabilizing a particular phase among the competing RSb_2 structures.

Figure 4(b) compares the phonon density of states (DoS) of the Sm-type and Yb-mono phases. Below the phonon band gap around 4.2 THz, two structures exhibit overall similar phonon DoS whereas the highest phonon bands of the Yb-mono phase lie lower in energy than those of the Sm-type phase, explaining the fact that under zero doping the free energy of the Yb-mono in Fig. 4(a) remains lower than that of the Sm-type with increasing temperature.

The highest frequency ($\gtrsim$4.2 THz) phonon branches, consist solely of Sb_c vibrations. Since the vibration modes are closely related to change of the stacking positions, they are further decomposed in Fig. 4(c) into in- and out-of-plane vibrations. The in-plane vibrations of Sb_c atoms mainly appear at high frequencies, indicating that the stacking sites of Sm-type and Yb-mono phases are dynamically stable.

D. Dynamical instability

1. Instability in the Yb-type phase

The phonon band structure of the Yb-type $LaSb_2$ phase in the conventional unit cell [Fig. 3(b)] shows two dynamical instability modes at the Γ point. To elucidate their underlying atomic origin, we display in Fig. 5(a) the in-plane and out-of-plane projected phonon DoS on the Sb_c atom. We find that the unstable phonon modes arise from the in-plane vibrations of the corrugated Sb_c atoms. The atomic displacements corresponding to the two unstable phonon modes are shown in Figs. 5(b) and 5(c). In both unstable modes, the Sb_c atoms on adjacent La-Sb corrugated layers exhibit reversed displacements, leading to lateral glide of the stacking sites from Y^0

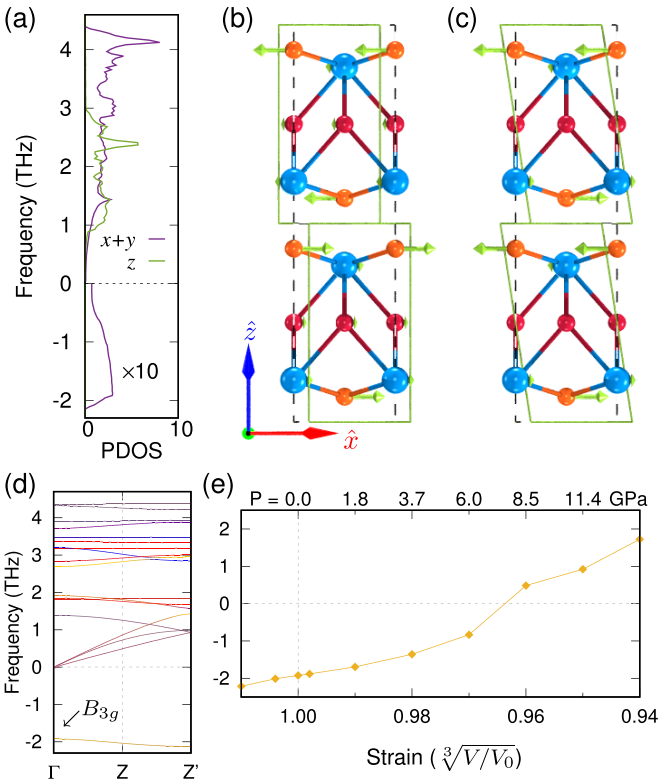

FIG. 5. Dynamical instability of Yb-type $LaSb_2$ at equilibrium volume. (a) Projected phonon DoS on the corrugated Sb_c atom. Purple and green solid lines denote in-plane and out-of-plane vibration projections, respectively. The imaginary frequencies of the unstable modes, plotted as negative values, are magnified by one order. (b), (c) Illustrations of the two unstable modes at the Γ point [Fig. 3(b)]. Green arrows denote atomic displacements corresponding to the eigenmodes, which are dominated by Sb_c atoms moving along $\hat{x}$. The dynamical instabilities are thus related to the saddle point stacking. See main text for details. (d) Phonon band dispersion of Yb-type phase along the Γ-*Z*-*Z*' symmetry directions [Fig. 3(b)] in primitive cell. (e) Phonon frequency of the B_{3g} mode versus hydrostatic pressure.

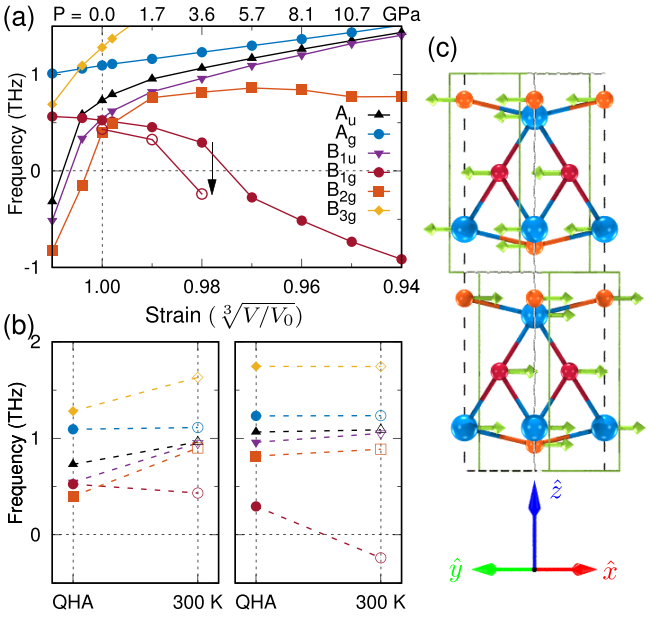

FIG. 6. Pressure-induced dynamical instability of Sm-type $LaSb_2$. (a) Optical-phonon-mode frequencies at the Γ point as a function of hydrostatic pressure. The B_{1g} mode softens under pressure, resulting in dynamical instability above 4.6 GPa. Open circles are self-consistent-phonon frequencies of the B_{1g} mode at 300 K. (b) Correction of the Γ point phonon frequencies using the quasiharmonic approximation (QHA) to finite temperature of 300 K. Left (right) panel is at the equilibrium (compressed $\sqrt[3]{V/V_0} = 0.98$) volume. (c) The B_{1g} mode projected on the (110) plane that corresponds to a slippage of the QL along the energy-map valley.

to either Y^+ or Y^-. These two paths are marked as ① and ② in Fig. 1(c). In the first mode [Fig. 5(b)], the upper QL block laterally glides opposite to the lower one resulting in the Yb-alt phase, while in the second mode [Fig. 5(c)], both QL blocks glide in the same direction resulting in Yb-mono phase. Note that the phonon bands in Fig. 3(b) are calculated in the conventional cell, which is twice as large as the primitive cell. Therefore, the number of phonon bands are doubled as well as the number of unstable modes at the Γ point. Figure 5(d) displays the phonon bands along the $\hat{k}_z$ direction of the primitive cell [see Fig. 3(b) for the labels Γ-Z-Z'], where the sole unstable mode is of B_{3g} irreducible representation. The two unstable modes at the Γ and *Z*' points of the primitive cell are folded into the two unstable modes at the Γ point of the conventional cell.

As discussed before, the Yb-type phase was speculated to be the high-pressure phase of $LaSb_2$ [12] as well as for $CeSb_2$ [8]. Even with the dynamical instability at equilibrium volume, the question rises whether this phase can become stable under hydrostatic pressure. Figure 5(e) shows the variation of frequency of the unstable B_{3g} mode under hydrostatic pressure. We find that this mode becomes stable under pressure higher than 8 GPa, which is, however, one order of magnitude higher than the experimental threshold pressure of 5 ∼ 12 kbar [11,12]. Therefore, the instability is predicted to persist after the pressure-induced structural transition, indicating that the Yb-type phase is unlikely to represent the high-pressure phase.

2. Instability in the Sm-type phase

The Sm-type phase does not exhibit a dynamical instability [see Fig. 3(a)] even though its stacking sites, $\cdots S^+S^- \cdots$, are also saddle points as in the Yb-type phase. Nevertheless, under hydrostatic tensile (compressive) pressure several (one) optical modes soften resulting into a dynamical instability as shown in Fig. 6(a). More specifically, the B_{1g} mode softens under compressive strain and a dynamical instability is predicted to emerge around 4.6 GPa. The B_{1g} mode, illustrated in Fig. 5(c), corresponds to a glide of the QL from the saddle points, S^+ and S^-, in the energy landscape in Fig. 1(c). If the system would follow the steepest descent paths ③ ($S^+ \rightarrow Y^+$) and ④ ($S^- \rightarrow Y^-$), then the Sm-type phase would undergo a structural transition to the Yb-alt ($\cdots Y^+Y^- \cdots$) phase, suggesting that the Yb-alt phase may represent the high-pressure state of the Sm-type bulk samples of $LaSb_2$. Note that this dynamical instability, calculated with zero doping, emerges

at a much higher pressure than the strain-induced transition above 0.05 electrons doping [Fig. 2(e)]. The combined effect of doping and strain to the dynamical instability and the consequent structural transition path from the Sm-type to a high-pressure state are thus an open question for a future study.

The softening of the B_{1g} mode under compressive strain is unusual in the sense that most optical modes soften under tensile strain, as seen in Fig. 6(a). Interestingly, the softening of the B_{1g} mode is further enhanced at higher temperatures. Figure 6(b) shows the effect of temperature on the frequencies of the optical modes at the Γ point, where solely the B_{1g} mode softens with increasing temperature. At the compressed volume [right panel of Fig. 6(b)], the instability can be induced even by temperature, which is a rather rare case. Note that the phonon-entropy-induced thermal expansion is not considered here, and the temperature-induced phonon instability can be understood as an effective pressure that might disappear if thermal expansion at finite temperature was taken into account.

IV. SUMMARY

First-principles electronic structure calculations revealed that various competing structural phases of the family of $R\mathrm{Sb}_2$ systems can be linked to different stacking sequences of consecutive QL building blocks. The energy landscape of the stacking position of two QLs depends critically on the rare-earth element as demonstrated for three prototype members $R\mathrm{Sb}_2$ (R = Sm, Yb, and La), where the energy minima and saddle points appear at distinct positions. The combination of sequential stacking sites naturally explains not only the well-known structures (Sm-type phase similar to SmSb_2 and Yb-type phase similar to YbSb_2), but also the MBE grown monoclinic phase (referred to as Yb-mono phase) as well as their relative total energies and dynamical instabilities. Our results show that the (i) charge doping, (ii) hydrostatic pressure, and (iii) phonon entropy can tune selectively the relative stability among the various phases; the Sm-type phase is stabilized under electron doping, while phonon entropy promotes the Yb-mono phase at high temperature. This reconciles the seemingly contradictory experimental findings of the recently discovered monoclinic phase of LaSb_2 and the previously reported Sm-type phase. The results also support our previous speculation that the Yb-mono phase may represent the high-pressure phase of LaSb_2, relevant to superconducting behavior in this family of materials. The proposed construction of the relative lateral shift of QL blocks paves a novel way to comprehend the various structural phases in this family of materials that hopefully extends to magnetic systems exhibiting complex magnetic phase transitions.

ACKNOWLEDGMENTS

The work at CSUN is supported by the NSF-PREP CSUN/Caltech-IQIM Partnership (Grant No. 2216774) and the NSF-Partnership in Research and Education in Materials (PREM) (Grant No. DMR-1828019). Part of the calculations were carried out in an Advanced Beowulf Cluster funded by the NSF Grant No. DMR-2406524. J.F. acknowledges funding provided by the Air Force Office of Scientific Research (Grant No. FA9550-22-1-0463), the Gordon and Betty Moore Foundation's EPiQS Initiative (Grant No. GBMF10638), and the Institute for Quantum Information and Matter, a NSF Physics Frontiers Center (NSF Grant No. PHY-2317110).

DATA AVAILABILITY

The data that support the findings of this article are not publicly available. The data are available from the authors upon reasonable request.

[1] R. Wang, R. Bodnar, and H. Steinfink, The structure of YbSb_2, a ZrSi_2 isotype, Inorg. Chem. **5**, 1468 (1966).

[2] R. Wang and H. Steinfink, The crystal chemistry of selected AB2 rare earth compounds with selenium, tellurium, and antimony, Inorg. Chem. **6**, 1685 (1967).

[3] F. Hulliger, Chapter 33 rare earth pnictides, in *Non-Metallic Compounds–II*, Handbook on the Physics and Chemistry of Rare Earths Vol. 4 (Elsevier, Amsterdam, 1979), pp. 153–236.

[4] A. Llanos, G. Campisi, V. Show, J. Kim, R. Dorrian, S. Salmani-Rezaie, N. Kioussis, and J. Falson, Monoclinic LaSb_2 superconducting thin films, Nano Lett. **24**, 8518 (2024).

[5] F. Hulliger and H. Ott, Superconductivity of lanthanum pnictides, J. Less-Common Met. **55**, 103 (1977).

[6] J. F. DiTusa, V. Guritanu, S. Guo, D. P. Young, P. W. Adams, R. G. Goodrich, J. Y. Chan, and D. van der Marel, Optical conductivity and superconductivity in LaSb_2, J. Phys.: Conf. Ser. **273**, 012151 (2011).

[7] J. A. Galvis, H. Suderow, S. Vieira, S. L. Bud'ko, and P. C. Canfield, Scanning tunneling microscopy in the superconductor LaSb_2, Phys. Rev. B **87**, 214504 (2013).

[8] O. P. Squire, S. A. Hodgson, J. Chen, V. Fedoseev, C. K. de Podesta, T. I. Weinberger, P. L. Alireza, and F. M. Grosche, Superconductivity beyond the conventional pauli limit in high-pressure CeSb_2, Phys. Rev. Lett. **131**, 026001 (2023).

[9] S. Guo, D. P. Young, P. W. Adams, X. S. Wu, J. Y. Chan, G. T. McCandless, and J. F. DiTusa, Dimensional crossover in the electrical and magnetic properties of the layered LaSb_2 superconductor under pressure: The role of phase fluctuations, Phys. Rev. B **83**, 174520 (2011).

[10] R. F. Luccas, A. Fente, J. Hanko, A. Correa-Orellana, E. Herrera, E. Climent-Pascual, J. Azpeitia, T. Pérez-Castañeda, M. R. Osorio, E. Salas-Colera, N. M. Nemes, F. J. Mompean, M. García-Hernández, J. G. Rodrigo, M. A. Ramos, I. Guillamón, S. Vieira, and H. Suderow, Charge density wave in layered $\mathrm{La}_{1-x}\mathrm{Ce}_x\mathrm{Sb}_2$, Phys. Rev. B **92**, 235153 (2015).

[11] S. L. Bud'ko, S. Huyan, P. Herrera-Siklody, and P. C. Canfield, Rapid suppression of charge density wave transition in LaSb_2 under pressure, Philos. Mag. **103**, 561 (2023).

[12] T. I. Weinberger, C. K. de Podesta, J. Chen, S. A. Hodgson, and F. M. Grosche, Pressure-dependent structural and electronic instabilities in LaSb_2, SciPost Phys. Proc. **11**, 018 (2023).

[13] I. Palacio, J. Obando-Guevara, L. Chen, M. Nair, M. G. Barrio, E. Papalazarou, P. Le Fèvre, A. Taleb-Ibrahimi, E. Michel, A. Mascaraque, and A. Tejeda, Fermi surface of LaSb_2 and direct

observation of a CDW transition, Appl. Surf. Sci. **610**, 155477 (2023).

[14] M. Ohno, M. Uchida, R. Kurihara, S. Minami, Y. Nakazawa, S. Sato, M. Kriener, M. Hirayama, A. Miyake, Y. Taguchi, R. Arita, M. Tokunaga, and M. Kawasaki, Quantum transport observed in films of the magnetic topological semimetal $EuSb_2$, Phys. Rev. B **103**, 165144 (2021).

[15] Y. Qiao, F. Wang, H. Wang, Z. Tao, Z. Jiang, Z. Liu, S. Cho, F. Zhang, Q. Meng, W. Xia, Y. Yang, Z. Huang, J. Liu, Z. Liu, Z. Zhu, S. Qiao, Y. Guo, H. Zhang, and D. Shen, Experimental observation of multiple topological nodal structure in $LaSb_2$, Sci. China Phys., Mech. Astron. **67**, 247411 (2024).

[16] F. Hulliger and R. Schmelczer, Crystal structure and antiferromagnetism of $EuSb_2$, J. Solid State Chem. **26**, 389 (1978).

[17] S. L. Bud'ko, P. C. Canfield, C. H. Mielke, and A. H. Lacerda, Anisotropic magnetic properties of light rare-earth diantimonides, Phys. Rev. B **57**, 13624 (1998).

[18] W. Tremel and R. Hoffmann, Square nets of main-group elements in solid-state materials, J. Am. Chem. Soc. **109**, 124 (1987).

[19] G. A. Papoian and R. Hoffmann, Hypervalent bonding in one, two, and three dimensions: Extending the Zintl–Klemm concept to nonclassical electron-rich networks, Angew. Chem. Int. Ed. **39**, 2408 (2000).

[20] R. Dorrian, J. Kim, A. Llanos, V. Show, M. Ohno, N. Kioussis, and J. Falson, Stacking-selective epitaxy of rare-earth diantimonides, Nano Lett. **25**, 11427 (2025).

[21] A. I. Acatrinei, D. Browne, Y. B. Losovyj, D. P. Young, M. Moldovan, J. Y. Chan, P. T. Sprunger, and R. L. Kurtz, Angle-resolved photoemission study and first-principles calculation of the electronic structure of $LaSb_2$, J. Phys.: Condens. Matter **15**, L511 (2003).

[22] D. P. Young, R. G. Goodrich, J. F. DiTusa, S. Guo, P. W. Adams, J. Y. Chan, and D. Hall, High magnetic field sensor using $LaSb_2$, Appl. Phys. Lett. **82**, 3713 (2003).

[23] P. C. Canfield, J. D. Thompson, and Z. Fisk, Novel Ce magnetism in Cedipnictide and Di-Ce pnictide structures, J. Appl. Phys. **70**, 5992 (1991).

[24] P. C. Canfield and Z. Fisk, Growth of single crystals from metallic fluxes, Philos. Mag. B **65**, 1117 (1992).

[25] P. C. Canfield, Solution growth of intermetallic single crystals: A beginner's guide, in *Properties and Applications of Complex Intermetallics* (World Scientific, Singapore, 2010), pp. 93–111.

[26] G. Kresse and J. Furthmüller, Efficient iterative schemes for *ab initio* total-energy calculations using a plane-wave basis set, Phys. Rev. B **54**, 11169 (1996).

[27] G. Kresse and J. Furthmüller, Efficiency of *ab-initio* total energy calculations for metals and semiconductors using a plane-wave basis set, Comput. Mater. Sci. **6**, 15 (1996).

[28] P. E. Blöchl, Projector augmented-wave method, Phys. Rev. B **50**, 17953 (1994).

[29] G. Kresse and D. Joubert, From ultrasoft pseudopotentials to the projector augmented-wave method, Phys. Rev. B **59**, 1758 (1999).

[30] A. Togo, L. Chaput, T. Tadano, and I. Tanaka, Implementation strategies in phonopy and phono3py, J. Phys.: Condens. Matter **35**, 353001 (2023).

[31] A. Togo, First-principles phonon calculations with phonopy and phono3py, J. Phys. Soc. Jpn. **92**, 012001 (2023).

[32] M. Zacharias and F. Giustino, One-shot calculation of temperature-dependent optical spectra and phonon-induced band-gap renormalization, Phys. Rev. B **94**, 075125 (2016).

[33] M. Zacharias and F. Giustino, Theory of the special displacement method for electronic structure calculations at finite temperature, Phys. Rev. Res. **2**, 013357 (2020).

[34] M. Zacharias, G. Volonakis, F. Giustino, and J. Even, Anharmonic lattice dynamics via the special displacement method, Phys. Rev. B **108**, 035155 (2023).

[35] In principle, the special displacement method can be combined with temperature-dependent relaxation of internal atomic coordinates. In the present work, this step was omitted due to computational constraints and is not expected to qualitatively affect the finite-temperature anharmonic phonon renormalization discussed here.

[36] See Supplemental Material at http://link.aps.org/supplemental/10.1103/t4m3-jjdn for the relaxed crystal structures and detailed lattice parameters.

[37] The single QL in vacuum preserves the tetragonal symmetry with a square lattice for R = Sm and La, but not for Yb, which prefers an orthogonal structure with a rectangular lattice. The tetragonal symmetry, however, is imposed on all three systems.

[38] F. Birch, Finite elastic strain of cubic crystals, Phys. Rev. **71**, 809 (1947).

[39] F. D. Murnaghan, The compressibility of media under extreme pressures, Proc. Natl. Acad. Sci. USA **30**, 244 (1944).

[40] A. Togo, L. Chaput, I. Tanaka, and G. Hug, First-principles phonon calculations of thermal expansion in Ti_3SiC_2, Ti_3AlC_2, and Ti_3GeC_2, Phys. Rev. B **81**, 174301 (2010).

[41] M. Born, Quantenmechanik der stoßvorgänge, Zeitschrift für Physik **38**, 803 (1926).